



Broadband time-resolved multi-channel functional near-infrared spectroscopy system to monitor in vivo physiological changes of human brain activity

Frédéric Lange, Francoise Peyrin, Bruno Montcel

► To cite this version:

Frédéric Lange, Francoise Peyrin, Bruno Montcel. Broadband time-resolved multi-channel functional near-infrared spectroscopy system to monitor in vivo physiological changes of human brain activity. *Applied optics*, 2018, 57 (22), pp.6417. 10.1364/ao.57.006417 . hal-01997861

HAL Id: hal-01997861

<https://hal.science/hal-01997861>

Submitted on 29 Jan 2019

HAL is a multi-disciplinary open access archive for the deposit and dissemination of scientific research documents, whether they are published or not. The documents may come from teaching and research institutions in France or abroad, or from public or private research centers.

L'archive ouverte pluridisciplinaire **HAL**, est destinée au dépôt et à la diffusion de documents scientifiques de niveau recherche, publiés ou non, émanant des établissements d'enseignement et de recherche français ou étrangers, des laboratoires publics ou privés.

Broadband time-resolved multi-channel functional near-infrared spectroscopy system to monitor *in vivo* physiological changes of human brain activity

FRÉDÉRIC LANGE, FRANÇOISE PEYRIN, AND BRUNO MONTCEL*

Université de Lyon; CREATIS; CNRS UMR5220; Inserm U1206; INSA-Lyon; Université Lyon 1, Université Jean Monnet Saint Etienne, Villeurbanne, France

*Corresponding author: bruno.montcel@univ-lyon.fr

Received 22 February 2018; revised 20 June 2018; accepted 21 June 2018; posted 22 June 2018 (Doc. ID 323340); published 26 July 2018

We have developed a broadband time-resolved multi-channel near-infrared spectroscopy system that can monitor the physiological responses of the adult human brain. This system is composed of a supercontinuum laser for the source part and of an intensified charge-coupled device camera coupled with an imaging spectrometer for the detection part. It allows the detection of the spectral, from 600 to 900 nm, and spatial dimensions as well as the arrival time of photon information simultaneously. We describe the setup and its characterization in terms of temporal instrument response function, wavelength sensitivity, and stability. The ability of the system to detect the hemodynamic response is then demonstrated. First, an *in vivo* experiment on an adult volunteer was performed to monitor the response in the arm during a cuff occlusion. Second, the response in the brain during a cognitive task was monitored on a group of five healthy volunteers. Moreover, looking at the response at different time windows, we could monitor the hemodynamic response in depth, enhancing the detection of the cortical activation. Those first results demonstrate the ability of our system to discriminate between the responses of superficial and deep tissues, addressing an important issue in functional near-infrared spectroscopy. © 2018 Optical Society of America

OCIS codes: (120.3890) Medical optics instrumentation; (120.4825) Optical time domain reflectometry; (120.6200) Spectrometers and spectroscopic instrumentation; (170.1470) Blood or tissue constituent monitoring; (170.2655) Functional monitoring and imaging; (170.6920) Time-resolved imaging.

<https://doi.org/10.1364/AO.57.006417>

1. INTRODUCTION

Functional near-infrared spectroscopy (fNIRS) is now a relevant neuroimaging tool to monitor the brain activation of adults or infants [1–3]. Although NIRS is increasingly used, functional magnetic resonance imaging (fMRI) is still considered to be the gold standard of imaging the brain's function [4–6]. However, even though this technique is non-invasive, some populations cannot be scanned. Indeed, the use of the strong magnetic field is a contraindication in patients with implanted electronic devices, like pacemakers or brain stimulators. There are also some difficulties in scanning a range of populations, such as claustrophobic people or people who have difficulties staying still for a long period of time, like children, infants, or the elderly. Finally, it requires a heavy instrument and a dedicated room. Contrary to fMRI, fNIRS provides a simple way to monitor all populations, including the ones incompatible with fMRI scans [7–9], without the movement restriction constraint. Thus, fNIRS enables the monitoring

of new tasks, in a daily life or ecological environment, that need free movement, like sports [10] or the monitoring of social interactions [11]. It can also operate in extreme conditions of acquisition, like for the monitoring of cerebral oxygenation during parabolic flight [12].

Besides those possibilities, one of the great advantages of fNIRS is the richness of the optical contrast of the cerebral activity. fMRI can access in an indirect manner the cerebral hemodynamics, from the deoxygenated hemoglobin concentration change ($\Delta[\text{HHb}]$) due to the blood-oxygenation-level-dependent (BOLD) effect [13]. Contrary to fMRI, fNIRS has the potential to directly access the cerebral hemodynamics due to the oxygenated and deoxygenated hemoglobin concentration changes, $\Delta[\text{HHb}]$ and $\Delta[\text{HbO}_2]$.

One of the main difficulties in fNIRS is to separate the systemic response due to the extracerebral layers from the response of the brain due to the activation itself [14]. Indeed, most groups are using continuous-wave (CW) systems [15] that are largely

influenced by the contribution of the superficial layers (skin, skull) [16,17]. Because of the wide use of CW systems, some methods using those systems have been developed to overcome this limitation. One of them uses short source-detector separation (SDS) [18,19]. This is based on the fact that in CW NIRS, the distance between the source and the detector determines the penetration depth of the light in the tissue [20]. Therefore, using a short SDS concurrently with a long SDS, one can regress the short signal, which is supposed to only probe the skin, from the long signal, which has probed both skin and brain. However, this technique still has some limitations. Indeed, it has been reported that the skin blood flow distribution varies a lot depending on the location [21]. So, using only a small region of the skin that is probed by the short SDS may not fully correct the skin response. There is also the issue of sweating that is not uniform across all of the skin. This issue is particularly important in sports applications. Moreover, it is worth noting that this technique uses the temporal domain to regress the short from the long channel. Thus, as it has been shown by Kirilina *et al.* [22], this could lead to an accidental removal of the cerebral signal itself because of the high correlation between the systemic artifact and the task-related cerebral response. A more recent work has shown that using a principal component analysis (PCA) Gaussian filter with a sufficient number of optodes can help to compensate for global systemic artifacts [23], overcoming the time correlation issue. However, those kinds of analysis require a large number of optodes, which is not always available.

Besides the CW systems, other techniques like time-resolved (TR) systems can be used [24–26]. TR systems provide more information than CW systems, which is a great benefit to improve the accuracy of NIRS, at the cost of a more complicated and expensive instrument [27]. These systems record the time of flight of photons, which indirectly codes the depth of penetration of the photons; by distinguishing the early from late photons, one can separate deep from superficial tissues. Thus, this technique can separate the superficial from deep layers with only one SDS, including all the tissues probed. This solves the issue of the contamination of the signal coming from the brain by the skin, which is an impediment to the expansion of NIRS because it questions its reliability, especially during exercise conditions [28,29].

However, even if TR systems are able to distinguish between those deep and superficial tissues with this technique, no direct correspondence can be made between the time of flight of photons and the real penetration depth. Thus, it could be good to consider another dimension in order to help to discriminate tissues, reinforcing the accuracy of this technique. In fact, it has been showed that the TR dimension coupled to the spectroscopic dimension could lead to an improvement of the accuracy [30,31]. In [30], Mottin and colleagues have shown that they could retrieve the variation of [HHb] and [HbO₂] in zebra finches using those two dimensions, even if the detection is extremely difficult due to the very weak contrast in those animals. In the context of human adult brain functional imaging, spectral signatures of the tissue's chromophores for all arrival times of photons can help to give a better knowledge of the photons' path in tissues. It is also helpful for determining the spectral signature of the physiological response.

The main goal of our work is to develop a NIRS system that is able to detect the richness of the cerebral activity more accurately by addressing the issue of skin contamination in the fNIRS signal [32].

Due to the benefits of TR systems to separate superficial from deep layers and the strength of a broadband system to resolve multiple chromophores, we have chosen to couple these two techniques.

We previously reported the first developments of the system [33]. In this paper, we first describe the instrumental setup. Then in Section 3, we describe the characterization of the system in terms of instrument response function (IRF), wavelength sensitivity, and stability. Finally, in Section 4, we report our first *in vivo* experiments during both a muscular cuff occlusion on the arm and during a cognitive task on the brain. This will demonstrate the ability of the system to retrieve hemodynamic changes and to discriminate between superficial and deep tissues. Finally, we discuss the possibilities of improvement of our approach both from a hardware and data processing point of view and explain how we could take advantage of all the information contained in our data.

2. SYSTEM SETUP

A. Overview

Figure 1 reports a schematic of the novel system developed at the CREATIS laboratory. The system is composed of a super-continuum laser (WhiteLase micro, Fianium UK) that provides picosecond pulses in the spectral range of 400–2200 nm. First the output beam of the laser is filtered in order to adapt the emitted bandwidth to the transmission window of tissue and to the detection bandwidth. We developed a low-pass filter with a cutting wavelength at 1000 nm. This filter is composed of a dichroic filter (DMSP1000, Thorlabs) that is followed by broadband mirror (BB1-E02, Thorlabs) that reflects the input light in the range 600–1000 nm. After the light has been reflected by this mirror, it passes through 2 mm of distilled water to eliminate remaining infrared (IR) wavelengths, particularly around 2 to 2.5 μm . We have not observed any thermal effects or damage to the tissue in any of our studies. The filtered beam is then injected into a homemade bundle by a FiberPort Connector (Thorlabs). This FiberPort Connector is composed of an achromatic lens, which couples the light with a FC/PC fiber connector. The power delivered onto the tissue by this emission fiber is about 12 mW for the 500–1000 nm bandwidth. A photodiode is placed behind the mirrors to monitor the power source stability. Homemade optical fiber bundles and headgear were designed to connect the emission and detection ports of the setup to the tissue. See Sections 2.B and 2.C for details about the bundles and headgear. It worth noting that we have not used a classical bandpass filter for safety reasons. Indeed, we could not find any filters that were characterized over such a large bandwidth. Therefore, we used water, which has a well-defined absorption spectrum, in order to be sure to block all the IR radiation.

The emergent light from the tissues is collected by the detection part, which is composed of an objective that focuses the light into an imaging spectrometer coupled with an intensified charge-coupled device (ICCD) camera. Basically, the

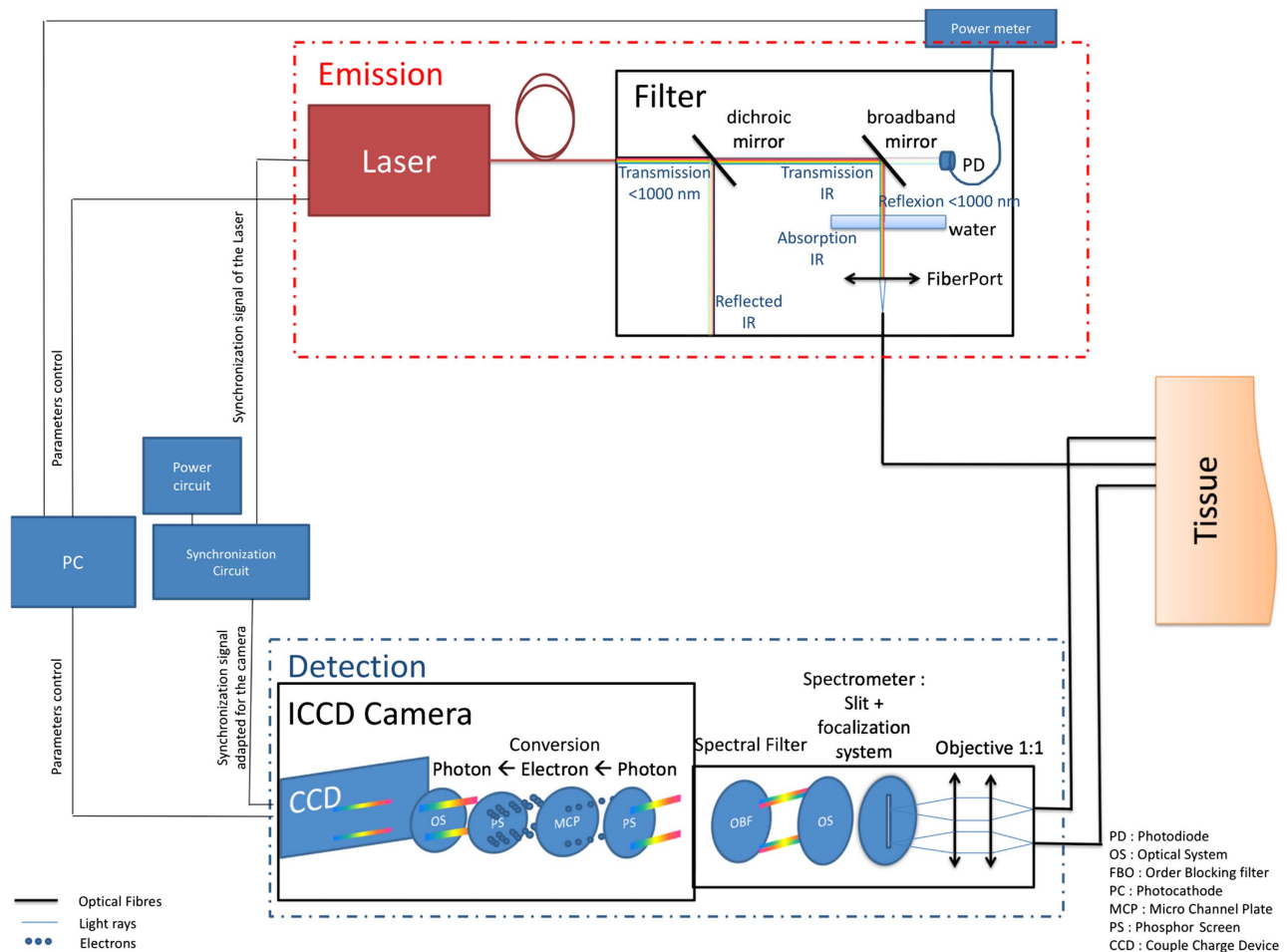


Fig. 1. Schematic of the system setup.

particularity of an ICCD camera is that an image intensifier is positioned in front of the CCD chip. The camera is highly sensitive and capable of high-speed gate operation (high-speed shutter), which gives the TR capability of the system. The detection optical fiber bundles are arranged vertically and fixed into a homemade 3D-printed fiber holder to fit the entrance slit of the spectrometer. To couple the light between the spectrometer and the optical bundles, an objective with unit magnification has been designed. It consists of an afocal montage composed of two achromatic lenses (49352INK, Edmund optics). A lens anodized aluminium holder has been designed to secure the lenses and fit into the C-mount entrance of the spectrometer. The spectrometer is an Inspector V10E (Specim, Finland). It covers a spectral range from 400 to 1000 nm (± 10 nm) with an entrance slit width of 150 μm and an effective slit length of 9.8 mm. It provides a spectral resolution of approximately 20 nm. The imaging spectrometer is mounted onto the camera via a C-mount adapter. An order-blocking filter is also inserted between the phosphor screen and the back of the spectrometer in order to prevent the second-order spectrum from overlapping with the end of the first-order spectrum. Then, the spectrally decomposed light enters the ICCD camera. Our ICCD camera provides a theoretical minimal time gate of 200 ps that can be delayed with a minimal time step

of 10 ps. It can be synchronized with the laser at a maximum of 2 Mhz and has a maximum acquisition frequency of 76 Hz.

The main advantage of this detection scheme (spectrometer + ICCD camera) is that we can simultaneously acquire the spectral and spatial information within a single time gate. Table 1 summarized the main system characteristics.

B. Optical Fiber Bundles

We have manufactured our own optical fiber bundles, which allow more flexible possibilities. For each bundle, source, or detector, we used graded index optical fibers with 100 μm core diameter (SEDI fiber, 100/140/250 VISNIR). These optical fibers with low modal dispersion reduce the broadening of the IRF. The size of the core is only slightly inferior to the size of the slit width of our spectrometer; this improves the optical coupling between the two. Depending on the application, we can adapt the length of the bundles, which could be useful in the future, during dual MRI/NIRS recordings, or in sports applications when the subject must be free and not restricted. For typical applications, we have developed 2 m long fibers. The source part consists of a bundle of eight optical fibers, which can be split into two (four in each distal point), if two sources are required. The power delivered is approximately 6 mW (in the 500–1000 nm range) per channel for the two-source configuration and 12 mW

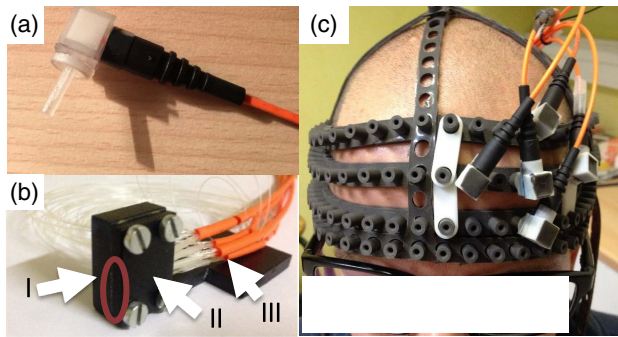


Fig. 2. Fibers/system interface. (a) Photograph of the fiber holder designed to hold the fibers on the head. (b) Photograph of the fiber holder on the camera end. Labels: I—Fibers' tips end arranged vertically to be imaged by the spectrometer slit. II—Fiber holder. III—Bundles of fibers coming from the head of the subject. (c) Photograph of the designed headgear that hold five fibers on the prefrontal cortex of the subject.

for the single-source configuration. For the detection part, we can adapt the number of optical fibers per bundle to adapt the signal-to-noise ratio (SNR). For typical applications, we use four optical fibers per bundle. Concerning the fiber connections, homemade 3D-printed connectors have been designed to connect the fibers to the scalp. It allows a 90° bending of the fibers in order to have a more secure and easy way to install the optodes. The source optodes are connected to the emission part of the setup with a typical FC/PC connector. The detection optodes are connected to the detection part of the setup with a homemade 3D-printed piece that allows a vertical arrangement of all the detection points in front of the slit of the spectrometer. To secure the fibers to the scalp, a special headgear has been designed. These connectors and headgear can be seen in Fig. 2.

C. Headgear Design

One of the main practical issues of NIRS is the placement of the optodes on the head. Indeed, the fiber contact is essential for a good quality of data. Thus, a special headgear has been designed. The main specifications that we wanted to achieve for the headgear were that it: is light and comfortable for the subject, allows precise positioning of the probes, is easily positioned, fixes the probes so there is no motion during the measurement, and allows an easy clearing of the hair. Thus, we built a homemade helmet with those specifications. It is made of a black caoutchouc (Ray Tech Magic Rubber). We used liquid caoutchouc that we could mold to a specific shape. We designed the mold and 3D-printed it. Finally, A 3D-printed part was designed to secure the different strips, which allows it to be adapted to different head sizes. This helmet applied to all our conditions. It can be seen in Fig. 2(c). All subjects reported that it is sufficiently light and comfortable. It provides a good fixation of our optodes and provides a framework for placing the optodes in a 1 × 1 cm grid anywhere on the head. It provides a way to have reproducible optode positions between subjects using the international 10/20 system [34].

D. Acquisition Sequence

One of the drawbacks of the ICCD camera is the dead time when electronically delaying the time gate (approximately

300 ms). This is incompatible with a fast functional measurement. So, we have developed two different strategies to tackle this problem.

1. Static Condition

The static condition is used when the acquisition rate is not an issue, for example, when characterizing the optical properties of tissue before the functional measurement, or to acquire the IRF. Thus, the long dead time is not an issue and a high SNR, fine temporally resolved temporal point spread function (TPSF) can be acquired. Here we chose the narrowest gate width (200 ps) and delayed it with a time step of 50 ps. This gives a time of flight resolution of 50 ps for this measurement. Figure 3 represents a typical image of the static condition.

2. Dynamic Condition

The dynamic condition is employed when performing the measurement of the functional run. For this condition, the time of flight resolution of the measurement is degraded as compared to the static condition to avoid too long an experimental duration. Typically, we take a maximum of eight points on the TPSF. We can acquire those points of the TPSF with different strategies. Here we describe the one used in the current work, and we will suggest other possibilities in the discussion.

The strategy employed here to acquire those eight points is to repeat the paradigm for each point in the TPSF. Thus, it induces a dead time between two points in order to electronically delay the gate of the ICCD and save the data. For this strategy, we assume that the response of the extra cerebral layers can change only due to the task but that it stays stable during the whole experiment. This is a reasonable hypothesis when the task is not physically demanding. In Fig. 3, this first strategy is illustrated with the placement of each gate.

E. Data Processing

In order to calculate the concentration changes during the *in vivo* experiment, we have used a method proposed by Montcel *et al.* [24]. This method is based on the modified Beer–Lambert law [35], adapted to take into account the path length for each arrival time of the photons. Moreover, we used the path length measured for each wavelength. Hence, we solved the equation

$$\Delta A_{T-T_0}(g) = \Gamma \cdot \Delta C_{T-T_0}(g) \cdot t(g) \quad (1)$$

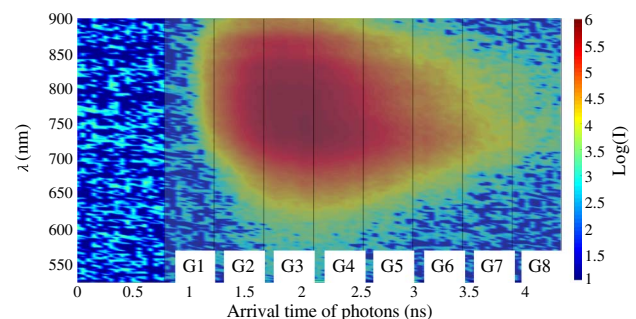


Fig. 3. Typical image of the static condition. The horizontal axis represents the time of flight of photons, the vertical axis, and the wavelength axis. The shadow boxes (G1: Gate 1) represent the position of the gates for the dynamic condition.

using a least-squares method. All the analysis was conducted with MATLAB (Mathworks, Natick, Massachusetts).

In Eq. (1), $A_{T-T_0}(g)$ is the attenuation change between the averaged signal of the rest period T_0 and the signal at time T within the gate; g , Γ is the matrix of the extinction coefficients of the chromophores at every wavelength, multiplied by the speed of light in tissue; $C_{T-T_0}(g)$ is the concentration change matrix of the chromophores for each g ; and $t(g)$ is the mean time of flight of photons at every wavelength, within g . The fitting was done over the range 700–900 nm, using the specific extinction coefficient spectra provided by Kolyva *et al.* [36]. It is worth noting that we subtract from every raw image what we call a dark image, which is an image acquired without any source fiber on, in order to get rid of the environmental noise. Moreover, the intensities' data were low-pass filtered with a moving average filter over a 2 s window to remove heartbeat oscillations and high-frequency noise.

In addition to the concentration changes, we have calculated the contrast and the contrast to noise ratio (CNR) for the brain activation experiment. The contrast is calculated as follows:

$$C(\lambda, g, T) = \frac{I(\lambda, g, T) - I_0(\lambda, g)}{I_0(\lambda, g)}. \quad (2)$$

Here, $I(\lambda, g, T)$ is the intensity at the time T of the experiment for g and the wavelength, λ ; and $I_0(\lambda, g)$ is the mean intensity along T during the rest condition for g and λ . The CNR for every gate and wavelength is defined as

$$\text{CNR}(\lambda) = \frac{\langle C(\lambda, g)_{\text{Act}} \rangle}{\text{std}(C(\lambda, g)_{\text{Rst}})}, \quad (3)$$

where $\langle C(\lambda, g)_{\text{Act}} \rangle$ is the mean contrast of the last 5 s of activation, and $\text{std}(C(\lambda, g)_{\text{Rst}})$ is the standard deviation of the rest period. These two metrics help to determine the best gates to consider; see Section 4.B for details.

3. SYSTEM CHARACTERIZATION

A. Instrument Response Function

The TPSF acquired is the convolution between the intrinsic response of the biological tissue probed and the IRF of the system. Therefore, one has to measure the IRF of the instrument in order to correct for it. The measurement of the IRF is recorded for each detector fiber prior to each measurement. This measurement is done by placing the source just in front of the detector with a neutral density filter and a sheet of white paper between them. The neutral density filter is used to reduce the light intensity and prevent damage to the camera. The sheet of white paper is placed in order to fill all the modes of the fiber [37]. A typical IRF can be seen in Fig. 4.

One can see the shift in the arrival time of the photons according to the wavelength. This is characterized by the mean arrival time of photons. The mean full width at half-maximum (FWHM) of the IRF for all wavelengths is 660 ps. This is rather large, taking into account the main theoretical contributions: 200 ps for the ICCD time gate, few tens of picoseconds (ps) for the laser. Other contributions from the electronic jitter of the trigger circuit and the modal dispersion into optical fibers have been explored. However, we were able to determine that this large IRF was due to the ICCD camera itself. Indeed, over a

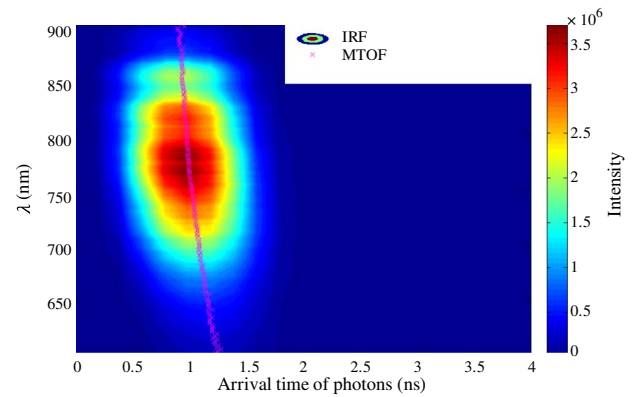


Fig. 4. Instrument response function (IRF) of the system. Typical IRF of the system from 600 to 900 nm. The pink dots represent the mean time of flight of photons (MTOF).

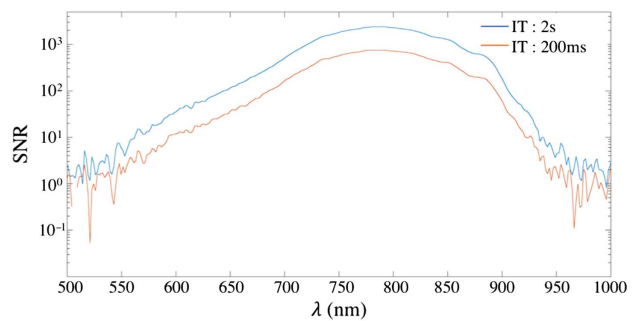


Fig. 5. SNR of the IRF as a function of wavelength for two different integration times: 2 s (blue) and 200 ms (red).

month, the mean width of the IRF broadened from 280 to 660 ps. We are monitoring this value, but it appears stable now. Nevertheless, even if this value is high, it is still in the range of the values reported in the literature [27]. The IRF also allows us to characterize the spectral sensitivity of our system. This spectral sensitivity can be seen in Fig. 5, which shows the SNR for two different integration times. One can see that the maximum sensitivity of our system is located at 810 nm. For an integration time of 200 ms, a SNR greater than 100 is obtained from 710 to 900 nm, and a SNR greater than 10 is obtained from 620 to 940 nm. These ranges can be extended by increasing the integration time. Given the good SNR between 700 and 900 nm, we decided to use that spectral band for the calculation in the *in vivo* experiments (see Section 4).

B. Warm-Up Time and Stability of the System

All parts of the setup require time to reach steady-state thermal equilibrium. We have tested the warm-up time required by the laser and the ICCD camera separately over 5 h. We determined that the power of the laser stays within 1% of variation after approximately 2 h. We also ensured that there was no wavelength-dependent variation of the laser power by acquiring the output spectrum for 5 h with an optical spectrometer (MayaPro; data not shown here). No wavelength-dependent effects were found, and the integrated output power was considered as a good metric of the laser power stability. It is worth

noting that the output power of the laser was continuously monitored and recorded during all experiments. If any drift had occurred, this power data would have been taken to normalize the data.

To characterize the ICCD camera, a mean of a dark image (front hand of the camera covered) has been taken as metric. The mean intensity of the dark image varies by less than 1% after about 1 h. So, we can conclude that the system needs about 2 h in order to reach its thermal stability.

The dark images give a raw characterization of the stability of the gate of the ICCD camera. Hence, to characterize the gate's stability more precisely, we recorded the IRF each hour for 8 h after the 2 h of warm-up. We focused on two parameters: the FWHM and the mean arrival time of the photons [38]. The mean arrival time of the photons, which illustrates the position of the gate, demonstrated a large variation of about 130 ps across 8 h. This would be problematic for a long acquisition time, as it would induce a drift in the recorded data. However, for a shorter time of less than an hour, the system is stable. The variation of the mean time of flight and of the FWHM is less than 15 ps. Since the measurements that we want to achieve with this system are not longer than 30 min, we consider this negligible.

C. Crosstalk and Dynamic Range

As all fibers are imaged in parallel on the same CCD array, crosstalk could arise between the detectors. However, we used a small number of detector fibers, which allowed us to greatly reduce the crosstalk. We have measured the crosstalk to be less than 1% between the time-independent signals of the detector bundles. This has been done by comparing the time-independent signal of the IRF at all the detectors when only one detector was illuminated. Moreover, we measured the dynamic range of our measurement to be of 3 orders of magnitude, which is in the range of previously reported systems [38]. Table 2 summarized the main system characterization.

Table 1. Summary of the System Parameters

Specifications	
Maximum number of sources	2
Maximum theoretical number of single-detector fibers	70
Repetition rate	1.2 MHz
Maximum output power of the source	≈12 mW
Maximum theoretical bandwidth	500–1000 nm
Maximum acquisition frequency	76 Hz
Minimum theoretical gate width	200 ps
Minimum time step	10 ps
Dead time between 2 gates	300 ms
Physical dimensions ($W \times L \times H$)	30 × 60 × 60 cm

Table 2. Summary of the System Characterization

Main Characteristic of the System	
IRF width	660 ps
IRF stability	±15 ps
Crosstalk	<1%
Spectral bandwidth	700–900 nm
Dynamic range	3 decades
Warm-up time	2 h

4. IN VIVO VALIDATION

In order to test our system, we have performed *in vivo* measurements based on well-established protocols that induce a change in the hemodynamic parameters. First, we have performed a muscular cuff occlusion, which induces large hemodynamic changes.

Second, we have tested the ability of our system to retrieve the brain activity, which induces smaller changes, during a mathematical task. The present study followed the policies of the Université Lyon 1 for the use of human healthy subjects in research. Informed consent was obtained for all subjects.

A. Cuff Occlusion

We performed an arterial cuff occlusion (300 mm Hg) on the left arm of a healthy male volunteer. We employed one source and one detector, with a source detector distance of 2 cm, located on the forearm. The protocol consisted of 5 min of baseline, followed by 5 min of arterial occlusion and 5 min of recovery. The measurement was performed in two steps. First the data were acquired for the static condition. Then we used this first measurement to properly position the gates that we used. In this experiment, we have used a single gate (3 ns width), equivalent to a CW measurement. This allows us to test the basic behavior of the instrument. We also used the static condition to be able to measure the path length of the photons within the arm. In addition, a set of dark images (i.e., without any source fiber emitting) are acquired after the acquisition sequence of the occlusion to get rid of the environmental noise during post-processing.

Here we used the method described in Section 2.E to calculate the concentration changes in $[\text{HbO}_2]$ and $[\text{HHb}]$. The measured path length was 6.7 cm at 800 nm, corresponding to a differential pathlength factor of 3.35, which is in accordance with the literature [39,40].

In Fig. 6 we can see the hemodynamic response for this experiment. We retrieve the classical response to an arterial cuff occlusion, with an increase in $[\text{HHb}]$ and a decrease in $[\text{HbO}_2]$. During the recovery, we observe the typical hyperaemia peak before the return to baseline. Moreover, the amplitudes match the one already reported in the literature [40,41].

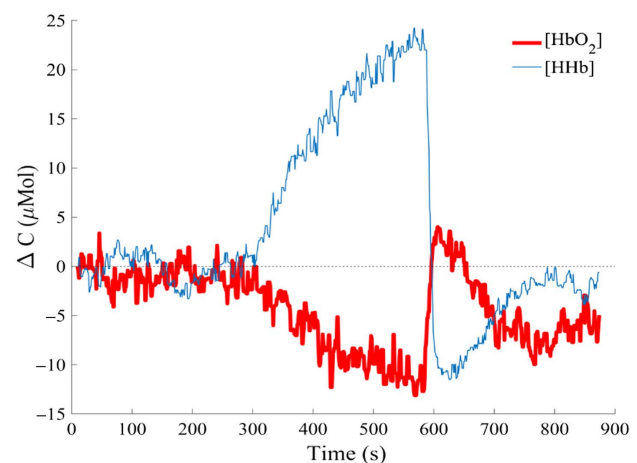


Fig. 6. Hemodynamic response to an arterial occlusion of the left arm of a healthy subject.

B. Brain Prefrontal Cortex Activation

We performed a measurement of a sequence of functional activation involving the prefrontal cortex. Here we present the results for a group of five healthy volunteers (four males, 25 ± 5 years), using one source and three detectors placed over the prefrontal cortex of the left hemisphere. The placement of the optodes can be seen on Fig. 8. The source detector distance is 2 cm for every channel. It covers the dorsolateral prefrontal cortex (DLPFC), which is involved in arithmetic tasks [40]. The measurement was performed, like the cuff occlusion, in two steps. First the data were acquired for the static condition when the subject was asked to stand still. Then we fixed eight delay times to sample the TPSF in the right time gate. Then we performed the recording of the activation sequence. During this sequence, the subject was asked to perform a simple calculation task (example: $15 + ? = 45$). The sequence consisted of 10 s of rest, followed by 15 s of activation and 15 s of recovery. This condition was repeated eight times, once per gate. This led to an acquisition sequence time of 6 minutes per run, which is an acceptable duration. We performed this sequence three times with an acquisition sample rate of 2 Hz, which led to a total time of about 18 min and to a number of 3 epochs per arrival time of the photons. In addition, a set of dark images was acquired before each condition in order to get rid of the environmental noise during post-processing.

Figures 7(a) and 7(b) show examples of the typical signals acquired on the forehead, with Fig. 7(a) showing a time-independent spectrum acquired on forehead (normalized by the spectral response of the IRF) and Fig. 7(b) showing a typical IRF and TPSF at 800 nm. Figure 7(c) shows the mean contrast of the last 5 s of activation at 800 nm for each gate for the same subject. Also shown on that figure is the CNR, defined in Section 2.E, at 800 nm. We can see that the contrast is increasing with the arrival time of the photons. This result is consistent with the literature [42–44] and stresses the ability of our system to differentiate superficial from deep tissues. Indeed, the cortical activation is occurring

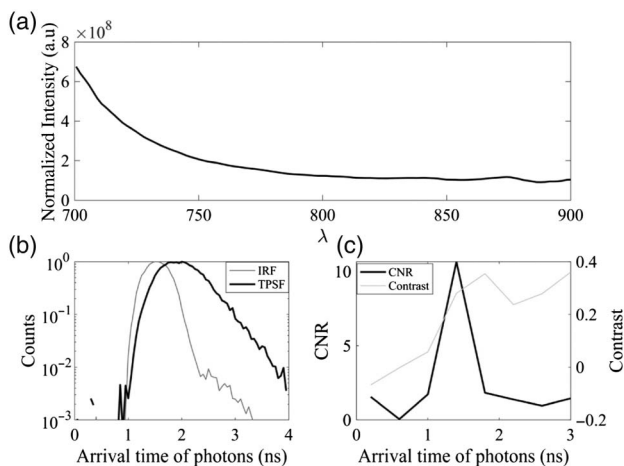


Fig. 7. (a) Typical time-independent spectrum acquired on the front head. The intensity has been normalized by the spectral response of the IRF. (b) Typical IRF (gray line) and TPSF (black line) at 800 nm acquired on the front head at a SD of 2 cm. (c) Example of contrast to noise ratio (black) and contrast (gray line) for all gates at 800 nm for subject 2.

deep in the tissue, in the cortex, so we expect to have a contrast that increases with the arrival time of the photons. A superficial activation would manifest as a maximum contrast in the first gates. Moreover, we can see in this example that the CNR is peaking for the fourth gate (time = 1.4 ns). This is explained by the high noise present in the last gates because the number of photons is extremely low in that region. After this contrast inspection, we calculated the concentration changes in hemoglobin only.

We analyzed the data using the method described in Section 2.E. To do so, we have considered two windows, by summing the photons acquired in the first gates (between gate 1 and 3, depending on subjects) for an early window, and the ones acquired in the last ones (between gate 4 and 8, depending on subjects) for a late window. Then the mean arrival time of the photons was calculated for each of the windows.

The choice of the inclusions of the different gates in those windows followed a two-step process. First, we have simulated the propagation of the photon in the tissue based on Monte Carlo simulations of the propagation of the light within a realistic head model (subject 4 of BrainWeb, <http://www.bic.mni.mcgill.ca/brainweb>), segmented in five tissue types [skin, skull, cerebrospinal fluid (CSF), gray matter (GM), and white matter (WM)]. We used the mesh-based Monte Carlo software to run the simulations [45]. Using the path length in each tissue type output by the simulation, we have calculated the sensitivity of the arrival time of the photons to each tissue type for a source-detector pair (2 cm) located on the prefrontal cortex. Figure 8 reports the histogram of the repartition of tissue types as a function of the arrival time of the photons. We can see that this repartition does not change rapidly, with a smooth transition between 0.5 and 1.5 ns regarding the main contribution of the skin/brain.

Second, we have matched the results of that simulation with the static condition acquired for all subjects. Depending on subjects, the arrival time of the photons in each gate differed slightly. In order to avoid the region between 0.5 and 1 ns, where the origin of the contrast is mixed between the skin

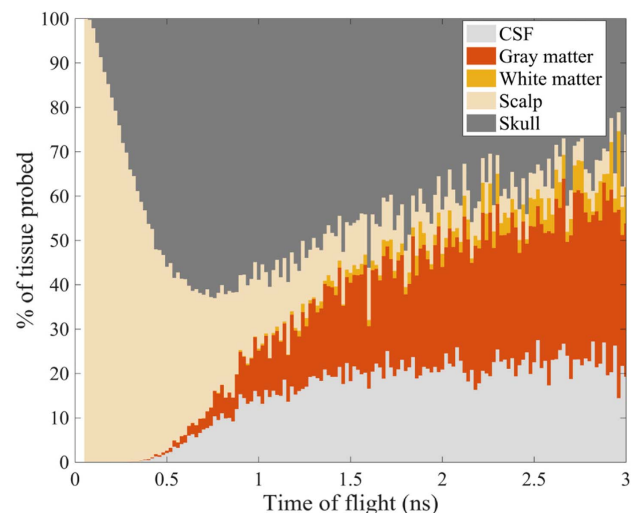


Fig. 8. Histogram of the repartition of tissue types (CSF, GM, WM, scalp, skull) as function as the arrival time of photons, for a detector positioned on the front head at 2 cm from the source.

and the brain, we needed to avoid including the third or fourth gate in some subjects.

Overall, in the case of the early window that we set, 69% of the tissue probed is skin, 30% is the skull, and the rest is CSF, white matter, and gray matter (less than 0.04 %). Therefore, we will assume that the responses within that window represent the skin's response in the following. In the late gate, only 12.5% is skin, but 15.6% is gray matter, the rest being mostly skull (52%) and CSF (18%). As we consider that those tissues have a negligible response during a functional paradigm, and that the gray matter part is prominent, we will assume that the responses within that window represent the brain's response in the following. Moreover, we have calculated a CW-like window by summing the signal acquired in all the gates and by using the mean arrival time of photons calculated from the static signal.

In Table 3, we report the mean variations of [HHb] and [HbO₂] over the last 2.5 s of the activation of the three runs, for all subjects and all channels and for the three windows: early, late, and CW-like. To identify channels with significant changes due to functional stimulation, the response of each channel for each subject was defined as the difference between the mean of the last 2.5 s window of activation and the mean of the 2.5 s window just prior to the activation. Paired *T*-tests were used to compare the responses of each channel for each five subjects to zero (i.e., no response). To be considered as a functional activation, the responses needed to present the typical activation pattern, defined as [HbO₂], being significantly superior compared to the baseline, and the [HHb] being significantly inferior to the baseline. *p* < 0.05 was considered statistically significant. Channels presenting a significant activation pattern are given in bold in the table.

If we focus on the late window, which has a higher sensitivity to the brain, we can see that two out of five subjects presenting a typical activation pattern in two channels. We report in Fig. 9 a typical response of subject 4 for every window and channel. We can see in Fig. 9 that the distribution and the magnitude of the hemodynamic responses over the skin is very different. This can be seen for optode 3, where the amplitude of the skin hemodynamics is big compared to the other optodes. The amplitude variation of the skin hemodynamics and the different time course over all the channels demonstrate that it is useful to monitor this response for each area probed. Indeed, we retrieve the classical activation pattern that was presented in most studies in the literature [46,47]. However, some studies reported a deactivation pattern [48,49] ([HHb] increases and [HbO₂] decreases) in the medial area of the anterior prefrontal cortex (APFC). This deactivation pattern is often reported as an artefact [25], but there is still some debate as to whether this is an actual neurophysiological process. As Pfturtscheller discussed, it could be explained in the context of "focal activation/surround deactivation." On two subjects, we could retrieve the decrease in [HbO₂] in the CW window. However, those responses were explained by the changes in the early windows, which demonstrated the same responses, but the late windows presented a classical increase in [HbO₂]. Those results are presented in Fig. 10. Those two examples could call into question the fact that this pattern is due to brain hemodynamics. However, to confirm that, we would need to place the position of the gates more rigorously. This will be

Table 3. Mean Hemodynamic Responses Over the Three Runs for All Subjects, All Channels, and for the Three Windows: Early Gate, Late Gate, and CW^a

		Subject 1		Subject 2		Subject 3		Subject 4		Subject 5	
		[HHb]	[HbO ₂]	[HHb]	[HbO ₂]	[HHb]	[HbO ₂]	[HHb]	[HbO ₂]	[HHb]	[HbO ₂]
C1	early late cw	-3.04 ± 0.31	-0.49 ± 0.68	-1.23 ± 0.74	4.61 ± 0.24	1.22 ± 0.17	0.67 ± 0.14	0.96 ± 0.69	0.67 ± 0.54	1.88 ± 0.74	0.59 ± 0.24
		-0.21 ± 0.04	0.34 ± 0.18	1.14 ± 0.13	3.19 ± 0.38	-0.01 ± 0.02	0.17 ± 0.08	-0.29 ± 0.05	0.73 ± 0.08	-0.29 ± 0.13	0.67 ± 0.38
		-0.82 ± 0.08	-0.37 ± 0.3	4.04 ± 0.26	10.92 ± 1.15	0.39 ± 0.09	0.63 ± 0.04	-0.29 ± 0.13	1.01 ± 0.18	-0.17 ± 0.33	1.00 ± 0.66
C2	early late cw	4.13 ± 0.88	3.98 ± 1.09	-4.87 ± 0.28	-1.21 ± 0.46	0.62 ± 0.28	0.91 ± 0.39	-0.74 ± 0.38	0.52 ± 0.60	0.15 ± 0.29	0.45 ± 0.46
		0.98 ± 0.09	0.88 ± 0.19	0.43 ± 0.05	0.73 ± 0.09	-0.01 ± 0.05	0.03 ± 0.15	-0.20 ± 0.10	0.30 ± 0.17	-0.29 ± 0.05	0.73 ± 0.09
		2.75 ± 0.31	6.5 ± 0.39	-15.94 ± 0.98	-8.74 ± 0.97	-0.03 ± 0.06	0.62 ± 0.17	-0.41 ± 0.24	0.52 ± 0.40	-0.14 ± 0.08	0.30 ± 0.21
C3	early late cw	4.78 ± 0.37	3.25 ± 0.56	-6.46 ± 0.23	2.42 ± 0.14	1.88 ± 0.64	-0.04 ± 0.77	3.33 ± 4.21	1.04 ± 4.03	-0.1 ± 0.23	0.37 ± 0.14
		0.93 ± 0.11	1.28 ± 0.28	0.08 ± 0.10	4.47 ± 0.17	0.02 ± 0.08	0.17 ± 0.13	-0.49 ± 0.26	2.71 ± 0.71	-0.20 ± 0.10	0.30 ± 0.17
		3.33 ± 0.25	7.57 ± 0.51	-0.20 ± 0.41	4.27 ± 0.68	0.14 ± 0.09	0.49 ± 0.06	-0.08 ± 0.29	1.66 ± 0.43	-0.33 ± 0.09	0.49 ± 0.25

^aThe conditions showing a typical activation pattern (increase in [HbO₂] and decrease in [HHb], *p* < 0.05) are given in bold.

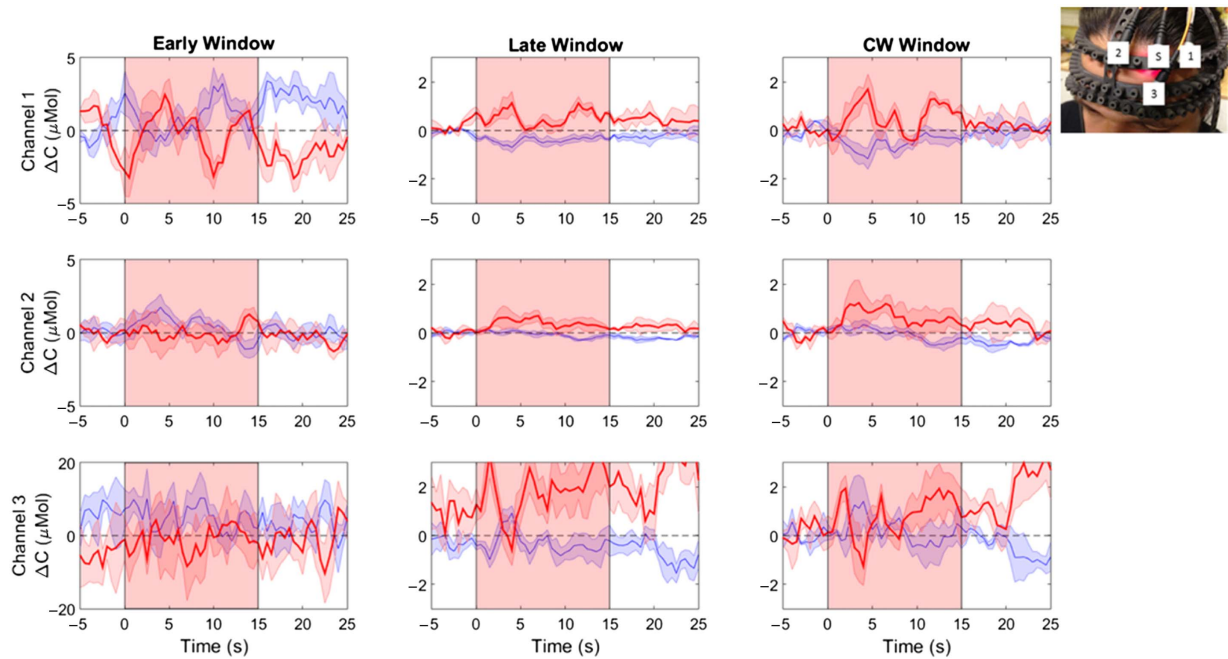


Fig. 9. Example of responses for subject 4, for every window (early window, late window, and CW-like window), and for every optode. The red thick line represents the $[HbO_2]$ concentration changes, and the blue thin line represents the $[HHb]$ concentration changes. The shadow regions represent the standard error of the mean across the 3 epochs. The red transparent boxes represent the activation period. The picture shows the positioning of every optode (S is the source).

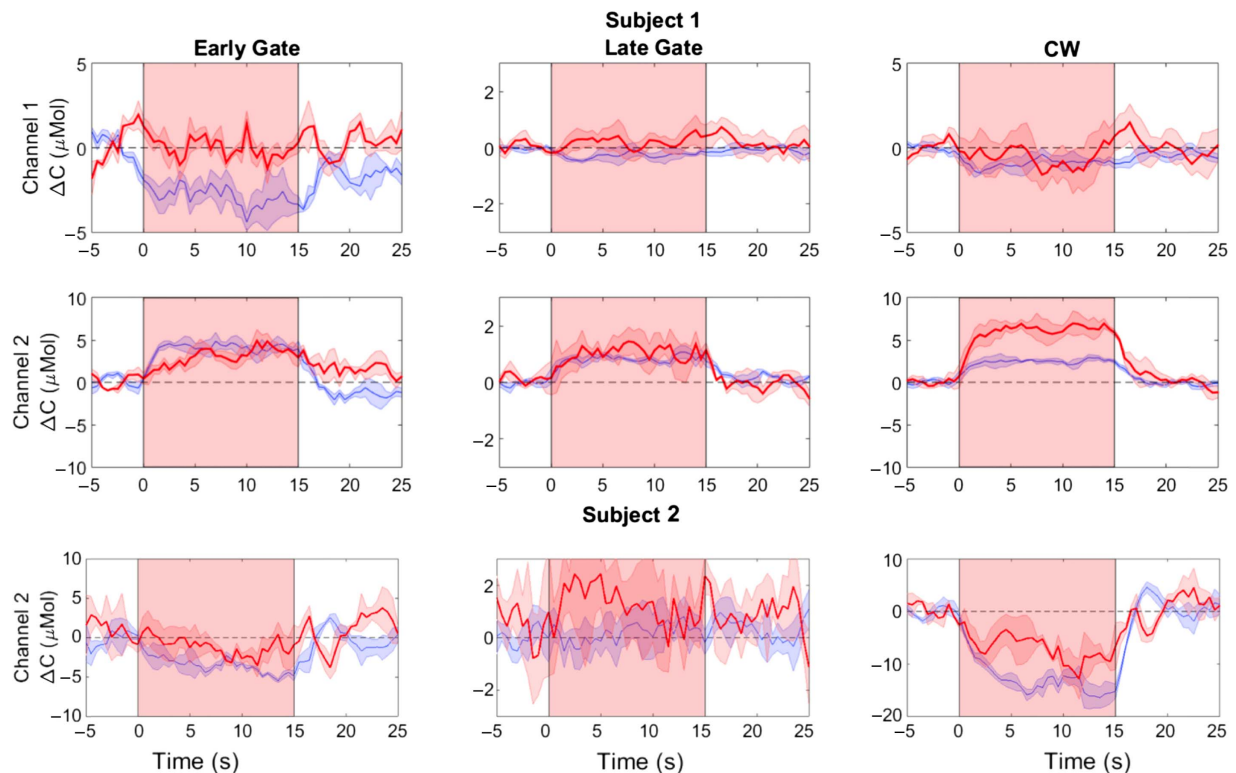


Fig. 10. Example of non-task-related cortical responses for subject 1 and 2. Upper and lower panel show the inverted $[HbO_2]$ responses for subject 1 and 2, and in channel 1 and 2, respectively. It shows the decrease in $[HbO_2]$ in the early and CW windows but an increase in $[HbO_2]$ in the late window. The middle panel shows the response of channel 2 of subject 1. It shows a global response in all of the windows with an increase in both $[HbO_2]$ and $[HHb]$. The red thick line represents the $[HbO_2]$ concentration changes, and the blue thin line represents the $[HHb]$ concentration changes. The shadow regions represent the standard error of the mean across the 3 epochs. The red transparent boxes represent the activation period.

discussed in Section 5. Indeed, when the systemic response is strong in the superficial layers, the late window can be still highly contaminated by the early one, as can be seen in Fig. 10. The middle part of that figure shows the response of optode 2 for subject 1. Here we can see that the three windows are showing the same response, with a large increase in $[\text{HbO}_2]$ and $[\text{HHb}]$, which corresponds to a systemic response.

5. DISCUSSION AND CONCLUSION

This work was aimed at reporting the first developments of a broadband TR fNIRS system that can detect the cerebral activity of human adults. This system is based on an ICCD camera coupled with an imaging spectrometer and a supercontinuum laser.

In this paper, we have described the instrumental setup and its characterization in terms of instrument response function (IRF), wavelength sensitivity, and stability. We have then reported its ability to retrieve hemodynamic responses during an arterial cuff occlusion in the arm, demonstrating its basic functions. Finally, we have demonstrated the ability of the system to detect the hemodynamic response during a cerebral activity induced by a cognitive stimulus.

The measurement of the functional brain activation allowed us to demonstrate the depth sensitivity of our system by showing that the contrast increases with the arrival time of the photons, which is consistent with the literature [42,43]. Although we retrieve the typical depth specificity of the TR instruments, we can use the information provided by our system to increase the accuracy of the depth determination. Indeed, using the gating capability of the system, we have been able to differentiate skin and brain responses, addressing the issues of systemic contamination and false positive and false negative responses [50]. In fact, the information retrieved by the TR systems gives us access to a more direct way to separate superficial and brain-related responses without using many optodes or risking blurring the brain response by the data processing technique used.

The separation of the different contributions of the hemodynamic signal is indeed of great interest. We have shown some discrepancies between the CW and TR hemodynamic responses for some subjects in the present study. However, we would have to look carefully at the gate positioning to have a more robust skin/brain separation. We considered an early and a late window as skin- and brain-sensitive, respectively, but we have seen that the late window was still probing a significant amount of the skin. Indeed, the current IRF of the system is rather large. Thus, the temporal smearing due to this large IRF implies that some of the photons having a long arrival time are sensitive to the shallow tissue. However, given the smooth change in tissue sensitivity at each arrival time of the photons shown in our simulation, this effect can be largely diminished by proper gate positioning. Thus, we would have to work on a more appropriate positioning of the gate to improve that separation.

Together with a better gate positioning, there are several perspectives to improve the system. We could first improve its light harvesting, which would improve the ability of the system to collect late photons and improve the quality of the spectrum. Indeed, it is worth noting that the sensitivity of our

system is lower than previously developed TR systems reported in the literature. For example, Liebert and colleagues reported a TR system capable of measuring TPSF with a very large source/detector distance separation (up to 9 cm), demonstrating the great sensibility of the system [51]. However, in the case of TR systems, this very large SDS is not mandatory in order to probe cerebral tissues [52], which is the primary goal of that system. Nonetheless, a better light harvesting method would improve the sensitivity of the system, especially to late photons. This could be done by first increasing the number of fibers. Indeed, we have only used four fibers by bundles so far because it was easier to handle at first. But we could greatly improve the number of fibers used, which would increase the SNR for each optode, and/or increase the number of optodes. Second, we could modify the objective and the optode bundles. We could use optical fibers with bigger cores, but we would have to go for step index (SI) fibers. Then, using a prism at the tip of the fibers, it could be possible to bend the light 90°, as it is now. On the detection side, the objective might be changed to perform a negative magnification, optimizing the light collection. The drawback of using SI fibers is that they would broaden the IRF, but we have seen that the width of the IRF is mainly due to the camera itself, so it should not be an issue.

Those SNR improvements, coupled with a better gate positioning, could even further improve the capabilities of the system. For example, it would be very beneficial in order to quantify a third chromophore, named cytochrome-c-oxidase (CCO) [53]. CCO is the terminal electron acceptor of the electron transport chain in the mitochondria, which is responsible for 95% of cellular oxygen metabolism. fNIRS can monitor the changes in the redox state of CCO using the oxidized minus reduced CCO spectra to obtain a measurement of changes in the concentration of oxidized CCO ($[\text{oxCCO}]$). Thus, this biomarker could be very interesting because it provides another and complementary way to evaluate neural activity [54].

In order to quantify the oxCCO together with the hemoglobin, one needs to use at least three wavelengths to be able to solve the modified Beer–Lambert law equation, although many more wavelengths are needed if one wants reliable results [55]. Ideally, it requires a broadband system, because the oxCCO has a broad spectrum over the range 700–900 nm, and its concentration is very low (i.e., about 10 times less than hemoglobin) [56]. Our system is then relevant for that particular application. Thus, the improvement of the SNR of the system would be very beneficial, especially (1) to better characterize the brain activation by getting access to the metabolic state of the tissue, and (2) to localize more efficiently the brain activity in depth, since the detection of cytochrome-c-oxidase has been shown as more brain-specific [56]. It worth noting that we have started to work on the $[\text{oxCCO}]$ detection with encouraging first results on cuff occlusion, and in a particular on a subject during the functional brain challenge presented in this paper. However, the current SNR of the system is not sufficient to consistently detect that signal on all subjects. Thus, we plan to upgrade the system with the above-mentioned improvements before attempting that detection.

Finally, it is worth mentioning that we are also developing an alternative method for the detection of the signal in different gates. This method is based on the work introduced by Selb

and collaborators [42] that enables the acquisition of all the delays in one CCD frame. This method uses special optical fiber bundles. In these bundles, we use fibers with different lengths in order to create a hardware delay. Thus, each fiber images a different time of flight for a given detector position, and there is no need to electronically delay the ICCD gates. Thus, combining a gate positioning optimization process with the multi-length fiber methods would greatly improve the system, because the acquisition frequency would be increased, and we could achieve a true simultaneous acquisition of all the dimensions. Indeed, if one wants to achieve a TR measurement of [oxCCO], it requires a multi-wavelength system, which is challenging for this type of instrumentation. One could use a streak camera for the detector, but it would be limited to the TR dimension with either the spectral [57] or spatial [58] dimension, but not both. Besides the streak cameras, the most widespread technology for TR measurement is time-correlated single-photon counting (TCSPC) [43]. Again, for this type of technology, one has to have one TCSPC per position or wavelength or use a multiplexing stage for the source or the detection [43]. Thus, we think that the use of the ICCD camera coupled with the spectrometer is relevant. Nevertheless, some groups have recently been developing a hyperspectral or multi-wavelength TR system based on TCSPC. Sekar and colleagues have reported a system [59] with a very large spectral bandwidth (600–1350 nm) that is mainly used to characterize tissue composition. Dunne and colleagues have reported a multi-spectral system that can acquire up to 16 wavelengths with an acquisition time compatible with functional studies. Indeed, that system has been designed to be able to measure the absolute concentration of [oxCCO] in the brain [40,60,61]. Those systems demonstrate that the use of the spectral information, coupled with the TR information, can be a great asset whether for fine tissue characterization or for the detection of supplementary contrasts. We think that the great amount of information acquired by such TR systems coupled with the recent developments in optoelectronics will push the use of TR systems in the future [62,63].

In conclusion, this paper has presented the first developments of a broadband TR multi-channel NIRS system to monitor human brain activity. Our first *in vivo* results are encouraging and demonstrate the ability of our system to detect the hemodynamic response as a function of depth. These results can be expanded to more important group studies and specific phantom studies, and current developments are ongoing in order to improve the capabilities of the system.

Funding. LABEX PRIMES (ANR-11-IDEX-0007, ANR-11-LABX-0063); France Life Imaging.

Acknowledgment. We thank the Optics Laboratory for the use of their equipment. This work was supported by the LABEX PRIMES of Université de Lyon, within the program “Investissements d’Avenir” operated by the French National Research Agency (ANR). This work was supported by France Life Imaging (FLI). The authors thank Stéphane Martinez from the mechanical workshop of the university Claude Bernard Lyon 1 for his help regarding some mechanical parts of the system. The authors also thank Manuel Khun and

Nadine Noel and “the pole de prototypage rapide” of the INSA Lyon for their help and for the impression of the 3D-printed part.

REFERENCES

1. M. Wolf, M. Ferrari, and V. Quaresima, “Progress of near-infrared spectroscopy and topography for brain and muscle clinical applications,” *J. Biomed. Opt.* **12**, 62104 (2007).
2. W. Lichty, K. Sakatania, Y. Xie, and H. Zou, “Application of near-infrared spectroscopy to investigate brain activity: clinical research,” *Proc. SPIE* **4082**, 4082–4086 (2000).
3. D. Boas, C. E. Elwell, M. Ferrari, and G. Taga, “Twenty years of functional near-infrared spectroscopy: introduction for the special issue,” *Neuroimage* **85**, 1–5 (2014).
4. B. R. Rosen and R. L. Savoy, “fMRI at 20: has it changed the world?” *Neuroimage* **62**, 1316–1324 (2012).
5. E. Bullmore, “The future of functional MRI in clinical medicine,” *Neuroimage* **62**, 1267–1271 (2012).
6. R. A. Poldrack, “The future of fMRI in cognitive neuroscience,” *Neuroimage* **62**, 1216–1220 (2012).
7. A. T. Eggebrecht, S. L. Ferradal, A. Robichaux-Viehoever, M. S. Hassanpour, H. Dehghani, A. Z. Snyder, T. Hershey, and J. P. Culver, “Mapping distributed brain function and networks with diffuse optical tomography,” *Nat. Photonics* **8**, 448–454 (2014).
8. T. Correia, S. Lloyd-Fox, N. Everdell, A. Blasi, C. Elwell, J. C. J. Hebden, and A. Gibson, “Three-dimensional optical topography of brain activity in infants watching videos of human movement,” *Phys. Med. Biol.* **57**, 1135–1146 (2012).
9. M. Smith, “Shedding light on the adult brain: a review of the clinical applications of near-infrared spectroscopy,” *Philos. Trans. R. Soc. A* **369**, 4452–4469 (2011).
10. S. Perrey, “Non-invasive NIR spectroscopy of human brain function during exercise,” *Methods* **45**, 289–299 (2008).
11. H. J. Spiers and E. A. Maguire, “Decoding human brain activity during real-world experiences,” *Trends Cogn. Sci.* **11**, 356–365 (2007).
12. S. Schneider, V. Abeln, C. D. Askew, T. Vogt, U. Hoffmann, P. Denise, and H. K. Strüder, “Changes in cerebral oxygenation during parabolic flight,” *Eur. J. Appl. Physiol.* **113**, 1617–1623 (2013).
13. R. B. Buxton, “Interpreting oxygenation-based neuroimaging signals: the importance and the challenge of understanding brain oxygen metabolism,” *Front. Neuroenerg.* **2**, 8 (2010).
14. D. Boas, A. M. Dale, and M. A. Franceschini, “Diffuse optical imaging of brain activation: approaches to optimizing image sensitivity, resolution, and accuracy,” *Neuroimage* **23**, S275–S288 (2004).
15. F. Scholkmann, S. Kleiser, A. J. Metz, R. Zimmermann, J. Mata Pavia, U. Wolf, and M. Wolf, “A review on continuous wave functional near-infrared spectroscopy and imaging instrumentation and methodology,” *Neuroimage* **85**, 6–27 (2014).
16. A. Liebert, H. Wabnitz, J. Steinbrink, H. Obrig, M. Möller, R. Macdonald, A. Villringer, and H. Rinneberg, “Time-resolved multidistance near-infrared spectroscopy of the adult head: intracerebral and extracerebral absorption changes from moments of distribution of times of flight of photons,” *Appl. Opt.* **43**, 3037–3047 (2004).
17. P. G. Al-Rawi, P. Smielewski, and P. J. Kirkpatrick, “Evaluation of a near-infrared spectrometer (NIRX 300) for the detection of intracranial oxygenation changes in the adult head,” *Stroke* **32**, 2492–2500 (2001).
18. L. Gagnon, R. J. Cooper, M. A. Yücel, K. L. Perdue, D. N. Greve, and D. Boas, “Short separation channel location impacts the performance of short channel regression in NIRS,” *Neuroimage* **59**, 2518–2528 (2012).
19. L. Gagnon, M. A. Yücel, D. Boas, and R. J. Cooper, “Further improvement in reducing superficial contamination in NIRS using double short separation measurements,” *Neuroimage* **85**, 127–135 (2014).
20. M. Patterson, S. Andersson-Engels, B. C. Wilson, and E. K. Osei, “Absorption spectroscopy in tissue-simulating materials: a theoretical and experimental study of photon paths,” *Appl. Opt.* **34**, 22–30 (1995).

21. Y. I. Satoru Kohno and Y. H. Satoru Kohno, "Temporal-spatial distribution of skin hemoglobin signals on the forehead during a verbal fluency task," in *FNIRS* (2014), p. 230.
22. E. Kirilina, A. Jelzow, A. Heine, M. Niessing, H. Wabnitz, R. Brühl, B. Ittermann, A. M. Jacobs, and I. Tachtsidis, "The physiological origin of task-evoked systemic artefacts in functional near infrared spectroscopy," *Neuroimage* **61**, 70–81 (2012).
23. X. Zhang, J. A. Noah, and J. Hirsch, "Separation of the global and local components in functional near-infrared spectroscopy signals using principal component spatial filtering," *Neurophotonics* **3**, 015004 (2016).
24. B. Montcel, R. Chabrier, and P. Poulet, "Time-resolved absorption and hemoglobin concentration difference maps: a method to retrieve depth-related information on cerebral hemodynamics," *Opt. Express* **14**, 12271–12287 (2006).
25. A. Jelzow, H. Wabnitz, I. Tachtsidis, E. Kirilina, R. Brühl, and R. Macdonald, "Separation of superficial and cerebral hemodynamics using a single distance time-domain NIRS measurement," *Biomed. Opt. Express* **5**, 1465–1482 (2014).
26. B. Montcel, R. Chabrier, and P. Poulet, "Detection of cortical activation with time-resolved diffuse optical methods," *Appl. Opt.* **44**, 1942–1947 (2005).
27. A. Torricelli, D. Contini, A. Pifferi, M. Caffini, R. Re, L. Zucchelli, and L. Spinelli, "Time domain functional NIRS imaging for human brain mapping," *Neuroimage* **85**, 28–50 (2014).
28. K. Byun, K. Hyodo, K. Suwabe, S. Kujach, M. Kato, and H. Soya, "Possible influences of exercise-intensity-dependent increases in non-cortical hemodynamic variables on NIRS-based neuroimaging analysis during cognitive tasks: Technical note," *J. Exerc. Nutr. Biochem.* **18**, 327–332 (2014).
29. C. Vignal, T. Boumans, B. Montcel, S. Ramstein, M. Verhoye, J. Van Audekerke, N. Mathevon, A. Van der Linden, and S. Mottin, "Measuring brain hemodynamic changes in a songbird: responses to hypercapnia measured with functional MRI and near-infrared spectroscopy," *Phys. Med. Biol.* **53**, 2457–2470 (2008).
30. S. Mottin, B. Montcel, H. G. de Chatellus, S. Ramstein, C. Vignal, and N. Mathevon, "Functional white-laser imaging to study brain oxygen uncoupling/recoupling in songbirds," *J. Cereb. Blood Flow Metab.* **31**, 393–400 (2011).
31. S. Mottin, B. Montcel, H. G. de Chatellus, S. Ramstein, C. Vignal, and N. Mathevon, "Corrigendum: functional white-laser imaging to study brain oxygen uncoupling/recoupling in songbirds," *J. Cereb. Blood Flow Metab.* **31**, 1170 (2011).
32. T. Takahashi, Y. Takikawa, R. Kawagoe, S. Shibuya, T. Iwano, and S. Kitazawa, "Influence of skin blood flow on near-infrared spectroscopy signals measured on the forehead during a verbal fluency task," *Neuroimage* **57**, 991–1002 (2011).
33. F. Lange, F. Peyrin, and B. Montcel, "A hyperspectral time resolved DOT system to monitor physiological changes of the human brain activity," in *Advanced Microscopy Techniques IV; and Neurophotonics II* (OSA, 2015), paper 95360R.
34. V. Jurcak, D. Tsuzuki, and I. Dan, "10/20, 10/10, and 10/5 systems revisited: their validity as relative head-surface-based positioning systems," *Neuroimage* **34**, 1600–1611 (2007).
35. A. Sassaroli and S. Fantini, "Comment on the modified Beer-Lambert law for scattering media," *Phys. Med. Biol.* **49**, N255–N257 (2004).
36. C. Kolyva, I. Tachtsidis, A. Ghosh, T. Moroz, C. E. Cooper, M. Smith, and C. E. Elwell, "Systematic investigation of changes in oxidized cerebral cytochrome c oxidase concentration during frontal lobe activation in healthy adults," *Biomed. Opt. Express* **3**, 2550–2566 (2012).
37. A. Liebert, H. Wabnitz, D. Grosenick, and R. Macdonald, "Fiber dispersion in time domain measurements compromising the accuracy of determination of optical properties of strongly scattering media," *J. Biomed. Opt.* **8**, 512–516 (2003).
38. J. Selb, B. B. Zimmermann, M. Martino, T. Ogden, and D. A. Boas, "Functional brain imaging with a supercontinuum time-domain NIRS system," *Proc. SPIE* **8578**, 857807 (2013).
39. A. Duncan, J. H. Meek, M. Clemence, C. E. Elwell, L. Tyszczyk, M. Cope, and D. Delpy, "Optical pathlength measurements on adult head, calf and forearm and the head of the newborn infant using phase resolved optical spectroscopy," *Phys. Med. Biol.* **40**, 295–304 (1995).
40. F. Lange, L. Dunne, and I. Tachtsidis, "Evaluation of haemoglobin and cytochrome responses during forearm ischaemia using multi-wavelength time domain NIRS," in *Advances in Experimental Medicine and Biology*, H. J. Halpern, J. C. LaManna, D. K. Harrison, and B. Epel, eds., *Advances in Experimental Medicine and Biology* (Springer, 2017), Vol. **977**, pp. 67–72.
41. S. J. Matcher, C. E. Elwell, C. E. Cooper, M. Cope, and D. T. Delpy, "Performance comparison of several published tissue near-infrared spectroscopy algorithms," *Anal. Biochem.* **227**, 54–68 (1995).
42. J. Selb, D. K. Joseph, and D. Boas, "Time-gated optical system for depth-resolved functional brain imaging," *J. Biomed. Opt.* **11**, 044008 (2006).
43. D. Contini, A. Torricelli, A. Pifferi, L. Spinelli, F. Paglia, and R. Cubeddu, "Multi-channel time-resolved system for functional near infrared spectroscopy," *Opt. Express* **14**, 5418–5432 (2006).
44. A. Abdalmalak, D. Milej, M. Diop, M. Shokouhi, L. Naci, A. M. Owen, and K. St. Lawrence, "Can time-resolved NIRS provide the sensitivity to detect brain activity during motor imagery consistently?" *Biomed. Opt. Express* **8**, 2162 (2017).
45. Q. Fang, "Mesh-based Monte Carlo method using fast ray-tracing in Plücker coordinates," *Biomed. Opt. Express* **1**, 165–175 (2010).
46. T. Limongi, G. Di Sante, M. Ferrari, and V. Quaresima, "Detecting mental calculation related frontal cortex oxygenation changes for brain computer interface using multi-channel functional near infrared topography," *Int. J. Bioelectromagn.* **11**, 86–90 (2009).
47. K. Mandrick, G. Derosiere, G. Dray, D. Coulon, J.-P. Micallef, and S. Perrey, "Utilizing slope method as an alternative data analysis for functional near-infrared spectroscopy-derived cerebral hemodynamic responses," *Int. J. Ind. Ergon.* **43**, 335–341 (2013).
48. G. Pfurtscheller, G. Bauernfeind, S. C. Wriessnegger, and C. Neuper, "Focal frontal (de)oxyhemoglobin responses during simple arithmetic," *Int. J. Psychophysiol.* **76**, 186–192 (2010).
49. G. Bauernfeind, R. Leeb, S. C. Wriessnegger, and G. Pfurtscheller, "Development, set-up and first results for a one-channel near-infrared spectroscopy system," *Biomed. Tech.* **53**, 36–43 (2008).
50. I. Tachtsidis and F. Scholkmann, "Publisher's note: false positives and false negatives in functional near-infrared spectroscopy: issues, challenges, and the way forward," *Neurophotonics* **3**, 039801 (2016).
51. A. Liebert, P. Sawosz, M. Kacprzak, W. Weigl, M. Botwicz, and R. Maniewski, "Time-resolved diffuse reflectance measurement carried out on the head of an adult at large source-detector separation," in *Annual International Conference of the IEEE Engineering in Medicine and Biology* (IEEE, 2010), Vol. **2010**, pp. 5784–5786.
52. A. Torricelli, A. Pifferi, L. Spinelli, R. Cubeddu, F. Martelli, S. Del Bianco, and G. Zaccanti, "Time-resolved reflectance at null source-detector separation: improving contrast and resolution in diffuse optical imaging," *Phys. Rev. Lett.* **95**, 078101 (2005).
53. G. Bale, C. E. Elwell, and I. Tachtsidis, "From Jöbsis to the present day: a review of clinical near-infrared spectroscopy measurements of cerebral cytochrome-c-oxidase," *J. Biomed. Opt.* **21**, 091307 (2016).
54. P. Phan, D. Highton, J. Lai, M. Smith, C. Elwell, and I. Tachtsidis, "Multi-channel multi-distance broadband near-infrared spectroscopy system to measure the spatial response of cellular oxygen metabolism and tissue oxygenation," *Biomed. Opt. Express* **7**, 4424–4440 (2016).
55. H. R. Heekeren, M. Kohl-Bareis, H. Obrig, R. Wenzel, W. von Pannwitz, S. J. Matcher, U. Dirnagl, C. E. Cooper, and A. Villringer, "Noninvasive assessment of changes in cytochrome-c oxidase oxidation in human subjects during visual stimulation," *J. Cereb. Blood Flow Metab.* **19**, 592–603 (1999).
56. C. Kolyva, A. Ghosh, I. Tachtsidis, D. Highton, C. E. Cooper, M. Smith, and C. E. Elwell, "Cytochrome c oxidase response to changes in cerebral oxygen delivery in the adult brain shows higher brain-specificity than haemoglobin," *Neuroimage* **85**, 234–244 (2014).
57. C. Abrahamsson, T. Svensson, S. Svanberg, S. Andersson-Engels, J. Johansson, and S. Folestad, "Time and wavelength resolved spectroscopy of turbid media using light continuum generated in a crystal fiber," *Opt. Express* **12**, 4103–4112 (2004).

58. C. V. Zint, W. Uhring, M. Torregrossa, B. Cunin, and P. Poulet, "Streak camera: a multidetector for diffuse optical tomography," *Appl. Opt.* **42**, 3313–3320 (2003).
59. S. K. V. Sekar, A. Dalla Mora, I. Bargigia, E. Martinenghi, C. Lindner, P. Farzam, M. Pagliazzi, T. Durduran, P. Taroni, A. Pifferi, and A. Farina, "Broadband (600–1350 nm) time-resolved diffuse optical spectrometer for clinical use," *IEEE J. Sel. Top. Quantum Electron.* **22**, 406–414 (2016).
60. L. Dunne, J. Hebden, and I. Tachtsidis, "Development of a near infrared multi-wavelength, multi-channel, time-resolved spectrometer for measuring brain tissue haemodynamics and metabolism," in *Oxygen Transport to Tissue XXXVI*, H. M. Swartz, D. K. Harrison, and D. F. Bruley, eds., *Advances in Experimental Medicine and Biology* (Springer, 2014), Vol. **812**, pp. 181–186.
61. F. Lange, L. Dunne, L. Hale, and I. Tachtsidis, "MAESTROS: a multi-wavelength time-domain NIRS system to monitor changes in oxygenation and oxidation state of Cytochrome-C-Oxidase," *IEEE J. Sel. Top. Quantum Electron.* **25**, 1–12 (2019).
62. D. Contini, A. Dalla Mora, S. Arridge, F. Martelli, A. Tosi, G. Boso, A. Farina, T. Durduran, E. Martinenghi, A. Torricelli, and A. Pifferi, "Time-domain diffuse optics: towards next generation devices," *Proc. SPIE* **9538**, 95380A (2015).
63. A. Pifferi, D. Contini, A. D. Mora, A. Farina, L. Spinelli, and A. Torricelli, "New frontiers in time-domain diffuse optics, a review," *J. Biomed. Opt.* **21**, 091310 (2016).